

Provided for non-commercial research and education use.
Not for reproduction, distribution or commercial use.



This article appeared in a journal published by Elsevier. The attached copy is furnished to the author for internal non-commercial research and education use, including for instruction at the authors institution and sharing with colleagues.

Other uses, including reproduction and distribution, or selling or licensing copies, or posting to personal, institutional or third party websites are prohibited.

In most cases authors are permitted to post their version of the article (e.g. in Word or Tex form) to their personal website or institutional repository. Authors requiring further information regarding Elsevier's archiving and manuscript policies are encouraged to visit:

<http://www.elsevier.com/copyright>



Contents lists available at ScienceDirect

Journal of Power Sources

journal homepage: www.elsevier.com/locate/jpowsour

Wavelet-transform-based power management of hybrid vehicles with multiple on-board energy sources including fuel cell, battery and ultracapacitor

Xi Zhang^a, Chris Chunting Mi^{a,*}, Abul Masrur^b, David Daniszewski^b

^a Department of Electrical and Computer Engineering, University of Michigan – Dearborn, 4901 Evergreen Road, Dearborn, MI 48128, USA

^b US Army RDECOM-TARDEC, Ground Vehicle Power & Mobility, 6501 E. 11 Mile Road, Warren, MI, USA

ARTICLE INFO

Article history:

Received 20 June 2008

Received in revised form 16 August 2008

Accepted 20 August 2008

Available online 27 August 2008

Keywords:

Hybrid electric vehicle

Wavelet transform

Wavelet decomposition

Power management

Power demand

Power flow

ABSTRACT

A wavelet-transform-based strategy is proposed for the power management of hybrid electric vehicles (HEV) with multiple on-board energy sources and energy storage systems including a battery, a fuel cell, and an ultra-capacitor. The proposed wavelet-transform algorithm is capable of identifying the high-frequency transient and real time power demand of the HEV, and allocating power components with different frequency contents to corresponding sources to achieve an optimal power management control algorithm. By using the wavelet decomposition algorithm, a proper combination can be achieved with a properly sized ultra-capacitor dealing with the chaotic high-frequency components of the total power demand, while the fuel cell and battery deal with the low and medium frequency power demand. Thus the system efficiency and life expectancy can be greatly extended. Simulation and experimental results validated the effectiveness of wavelet-transform-based power management algorithm.

© 2008 Elsevier B.V. All rights reserved.

1. Introduction

Fuel cells (FCs) have been considered as an alternative source of power for vehicle propulsion. As an alternative power source, FCs are environment friendly because they do not generate any harmful pollution. As energy converters, FCs are also more efficient than internal combustion engines (ICE) [1–2]. However, high cost and poor transient performance have restrained FCs from being used in large-scale vehicular applications. Due to the unidirectional power flow characteristics of the FCs, the energy from regenerative braking of a vehicle cannot be handled by FCs, hence vehicle efficiency enhancement is not possible through these devices alone. In addition, the size and lifetime of an FC may be dramatically impacted by the chaotic and rapid power demand variations of an HEV. Therefore hybridization of fuel cells with other energy storage devices, such as ultra-capacitors and batteries, are often necessary [3–5].

For systems containing multiple power sources or multiple energy storage systems, an appropriate power management algorithm is indispensable. Ref. [6] introduced a fuzzy logic supervisory-based power management strategy for a fuel cell/ultra-capacitor/battery combined electric vehicle. An adaptive control method for power sharing in hybrid FC/battery power sources was presented in [7]. These power management strategies

have been proven effective in dealing with system efficiency, but they fail to address the lifetime of the fuel cell stack due to negative impact of frequent and rapid load demand variations in real world drive cycles.

Ultra-capacitors (UCs) offer significantly better energy densities than do conventional capacitors. They are also highly suitable for the bulk of the transient power demands during acceleration and braking processes since the charge/discharge time of an UC can vary in a wide range [8–10], which ensures that the high efficiency and high durability of the UCs are fully employed, and the lifetime of the FC is extended because the UCs can handle lots of high and fast power outputs. Also, if there exists a battery pack in the HEV, the lifetime of the battery is extended as a result of not being subjected to many high-current charges or discharges. Delay of battery degradation is a major advantage for the combined battery/ultra-capacitor energy storage system (ESS). The wavelet-transform algorithm shows satisfactory performance in analysis and acquisition of high-frequency transients [11–14] (e.g. transient power demand variations during the drive cycles). So a wavelet decomposition algorithm is introduced in this paper for the power management of an HEV, where the UC deals with rapid-variation components of the total power demand of a HEV.

The incorporation of a battery with high energy density to the system not only solves the problem of unidirectional low-frequency-component power flow with the FC/UC configuration, but also reduces the size of the FC module since the output power is shared between the FC and battery. Moreover, the output voltage

* Corresponding author. Tel.: +1 313 583 6434; fax: +1 313 583 6336.
E-mail address: chrismi@umich.edu (C.C. Mi).

of the battery is less influenced by the load compared to a FC [15]. Therefore the battery can help stabilize the DC bus voltage and also make the power system more controllable.

In this paper, the Advanced Vehicle Simulator (ADVISOR) [27] tool is employed for modeling the power demand of the HEV. The Orange County Cycle (OCC) load power profile is chosen as an example to demonstrate the power demand during the drive cycle. First, the OCC power demand is decomposed into high- and low-frequency components by utilizing the wavelet transform. Then, the high-frequency components are assigned to the UC bank. The FC stack and battery pack share the low-frequency components. The battery absorbs the negative (regenerative) portion of power demand and the FC module carries the major portion in the positive part (including load power and battery/UC charging). Finally, simulation [28] and real time environment based experimental results verify that the power source modeling is correct, and the proposed wavelet-transform power management algorithm is valid.

2. System configuration

Fig. 1 shows a typical hybrid energy system consisting of an FC, a battery and a UC. A unidirectional DC/DC converter and two bi-directional DC/DC converters are directly connected to the FC, battery and UC, respectively. The power demand of the HEV can be satisfied by controlling the direction and amount of the output power (power-oriented-control) of each energy component. The optional bi-directional DC/DC converter placed between the DC bus and the load is for the purpose of voltage regulation to keep the DC load voltage stable. The required power of the FC, battery and UC is calculated by the proposed wavelet-transform-based algorithm.

The terminal voltage and output current of each power source, which help to obtain the instantaneous power, are sampled and provided as inputs to the data acquisition (DAQ) and control system for comparison with the desired power. The DC voltage on the load side is sampled and fed back to the DC load voltage regulator located in the DAQ and control system. The PWM signals generated from

the PID controllers are used to control the four DC/DC converters respectively for power tracking and voltage regulation. If there are only three DC/DC converters without the optional DC/DC converter connected between the load and DC bus, the DC load voltage can be stabilized by choosing the voltage-oriented-control for the converter connected to the battery considering its voltage robustness, and power-oriented-control for the other two converters connected to the FC and UC. If the state of charge (SOC) of the battery or UC falls below a predetermined threshold, the switch between the FC and the battery/UC is closed until the voltage returns within the desired limits.

The output current from the FC module is limited by its maximum value. The battery and UC are initially charged to sufficient voltage to ensure that the voltage difference between the FC and the battery or the UC is within an acceptable range when the switch turns on. This helps ensure that the surge current is within allowable limits and the membrane of the FC module is not damaged. The specific control process will be discussed in detail in Section 4.3.

3. Modeling of power sources

In order to develop and validate the proposed power management algorithm, the models of each component need to be developed.

3.1. Modeling of lithium-ion battery

Lithium-ion batteries are idea candidate for use in hybrid electric vehicles due to their high energy density, high power density, and long lifetime [16–18]. This paper uses a lithium-ion battery as a power source capable of absorbing the slow-variation stationary regenerative energy and assisting the FC to provide adequate power to the load.

The equivalent electrical schematic of a lithium-ion battery is shown in Fig. 2. It consists of an equilibrium potential E , an internal resistance having two components R_1 and R_2 and an effective

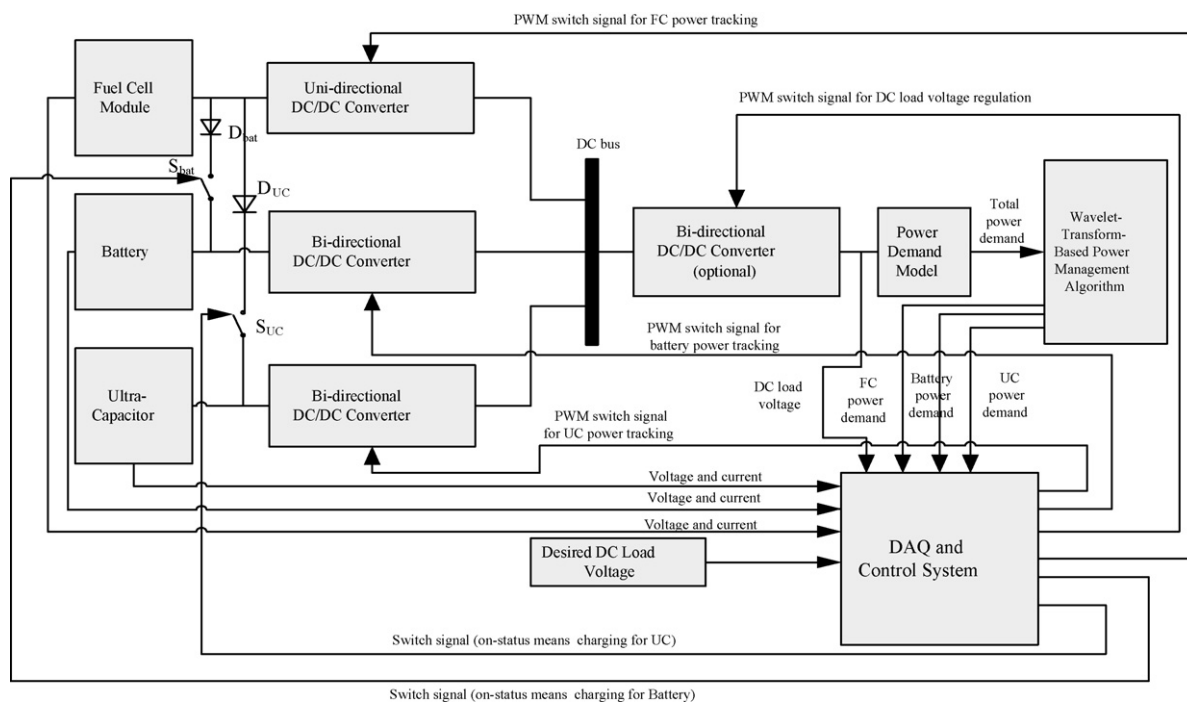


Fig. 1. System configuration of the multi-source hybrid vehicle power system.

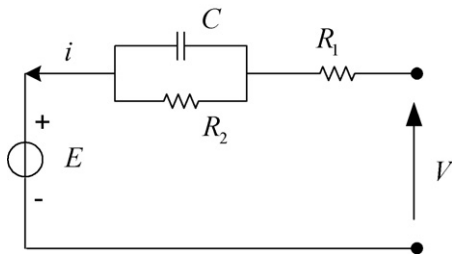


Fig. 2. Equivalent circuit model of the lithium-ion battery.

capacitance C characterizing the transient response of charge double layers.

The equilibrium potential of the battery depends on the temperature and the state of discharge (SOD). The reference discharge curve, reference rate and reference temperature are chosen based on experimental data. The equilibrium potential as a function of SOD is expressed as an n th-order polynomial. A potential correction term is used to compensate for the variation resulting from the ambient temperature change. Thus, the following equations are obtained to express the relationship among the potential, terminal voltage and SOD [19].

$$E[i(t), T(t), t] = v[i(t), T(t), t] - R_{\text{int}}i(t) \quad (1)$$

$$v[i(t), T(t), t] = \sum_{k=0}^n c_k \text{SOD}^k [i(t), T(t), t] + \Delta E(T) \quad (2)$$

$$\text{SOD}[i(t), T(t), t] = \frac{1}{C_r} \int_0^t \alpha[i(t)] \cdot \beta[T(t)] \cdot i(t) dt \quad (3)$$

where c_k is the coefficient of the k th order term in the polynomial expression for the reference curve and C_r is the battery capacity; ΔE expresses the potential correction term.

The battery temperature change is determined by the thermal energy balance expressed as [20]

$$m \cdot c_p \cdot \frac{dT(t)}{dt} = i(t)^2 \cdot R_1 + \frac{1}{R_2} [v(t) - E[i(t), T(t), t] - i(t)R_1]^2 - h_c A [T(t) - T_a] \quad (4)$$

where m is the battery weight; A is the surface area; c_p is heat capacity; h_c is cooling coefficient; T_a represents the ambient temperature.

3.2. Modeling of fuel cell

Proton exchange membrane fuel cells (PEMFCs) are considered to be promising for application as distributed generation sources due to high efficiency and compactness [1–2,21–24]. The PEMFC is also a primary candidate for environment-friendly vehicles.

The nomenclatures of the PEMFC are as follows: B and C , constants to calculate the activation over voltage [A^{-1}] and [V]; E_{cell} , Nernst cell voltage [V]; $E_{\text{d,cell}}$, overall effect of the fuel and oxidant delay [V]; $E_{0,\text{cell}}$, open cell voltage [V]; $E_{0,\text{cell}}^0$, standard reference potential per cell [V]; F , Faraday's constant [C kmol^{-1}]; I , FC current [A]; k_E , empirical constant in calculating open cell voltage [VK^{-1}]; k_{H_2} , hydrogen valve molar constant [$\text{kmol}(\text{atm s})^{-1}$]; k_{O_2} , oxygen valve molar constant [$\text{kmol}(\text{atm s})^{-1}$]; k_r , modeling constant [$\text{kmol}(\text{s A})^{-1}$]; N_0 , number of FCs in series; p_{H_2} , hydrogen partial pressure [atm]; p_{O_2} , oxygen partial pressure [atm]; $q_{\text{H}_2}^{\text{in}}$, hydrogen input flow [kmol s^{-1}]; $q_{\text{H}_2}^{\text{req}}$, required hydrogen flow for load change [kmol s^{-1}]; $q_{\text{O}_2}^{\text{in}}$, oxygen input flow [kmol s^{-1}]; $q_{\text{O}_2}^{\text{req}}$, required oxygen flow for load change [kmol s^{-1}]; R , gas constant [$\text{J}(\text{mol K})^{-1}$];

$r_{\text{H-O}}$, hydrogen–oxygen flow ratio; R_{ohm} , internal resistance [Ω]; T , FC stack temperature [K]; U , utilization rate; V_{act} , activation over voltage [V]; V_{ohm} , ohmic over voltage [V]; V_{out} , FC output voltage [V]; λ_e , constant factor in calculating $E_{\text{d,cell}}$ [Ω]; τ_e , overall flow delay [s]; τ_{H_2} , hydrogen time constant [s]; τ_{O_2} , oxygen time constant [s].

At the anode, three factors (hydrogen input flow, hydrogen output flow and hydrogen flow that reacts) determine the effective hydrogen partial pressure. The final expression for the hydrogen partial pressure is described as [22]

$$p_{\text{H}_2} = \frac{1/k_{\text{H}_2}}{1 + \tau_{\text{H}_2} s} (q_{\text{H}_2}^{\text{in}} - 2k_r I) \quad (5)$$

Similarly, the expression for the oxygen partial pressure is obtained as

$$p_{\text{O}_2} = \frac{1/k_{\text{O}_2}}{1 + \tau_{\text{O}_2} s} (q_{\text{O}_2}^{\text{in}} - k_r I) \quad (6)$$

The relationship among the FC output voltage V_{out} , Nernst cell voltage E_{cell} , activation voltage $V_{\text{act}} = B \ln(CI)$ and overall ohmic voltage $V_{\text{ohm}} = IR_{\text{ohm}}$ is delineated as [23]:

$$V_{\text{out}} = N_0 E_{\text{cell}} - B \ln(CI) - IR_{\text{ohm}} \quad (7)$$

where

$$E_{\text{cell}} = E_{0,\text{cell}}^0 - k_E(T - 298) + \frac{RT}{2F} \ln[p_{\text{H}_2} \cdot (p_{\text{O}_2})^{0.5}] - E_{\text{d,cell}} \quad (8)$$

$$E_{\text{d,cell}}(s) = \lambda_e I(s) \frac{\tau_e s}{\tau_e s + 1} \quad (9)$$

It should be noticed that the fuel cell voltage has to be kept at or below 0.9 V otherwise the Pt catalyst oxidizes and the platinum migrates. In this paper, the no-load voltage of the studied fuel cell is 0.6 V. That is to say, at any load, the fuel cell voltage will be at or below 0.6 V, so the aforementioned requirement is satisfied. Specific parameters and numerical analysis will be shown in Section 5.1.

A feedback from the FC module current is applied to control the hydrogen and oxygen flow rates according to the power demand

$$q_{\text{H}_2}^{\text{req}} = \frac{N_0 I}{2FU}, q_{\text{O}_2}^{\text{req}} = \frac{1}{r_{\text{H-O}}} q_{\text{H}_2}^{\text{req}} \frac{N_0 I}{2r_{\text{H-O}}FU} \quad (10)$$

The block diagram of the PEMFC model based on the above equations is shown in Fig. 3.

3.3. Modeling of ultra-capacitor

The classical equivalent electric model [8,9] of a UC cell is introduced as shown in Fig. 4. The circuit parameters are shown as follows: C , capacitance [F]; C_{UCbank} , total capacitance of the UC bank [F]; E , amount of energy flowed from the UC [W s]; n_1 , number of capacitors in series; n_2 , number of UC branches in parallel; R_{EPR} , equivalent parallel resistance [Ω]; R_{ESR} , equivalent series resistance [Ω]; V_0 , initial voltage [V]; V_f , final voltage [V].

As depicted in Fig. 3, the series resistance R_{ESR} is the charging/discharging resistance, and the parallel resistance R_{EPR} represents the self-discharging losses. However, R_{EPR} only has impact on the long-term energy storage performance.

The state of charge of the UC can be described as a percentage of the rated energy capacity, which depends on the terminal output voltage. The energy flowing out from the UC is directly determined by the capacitance and the voltage change as expressed in (11) [9,10].

$$E = \frac{1}{2} C (V_0^2 - V_f^2) \quad (11)$$

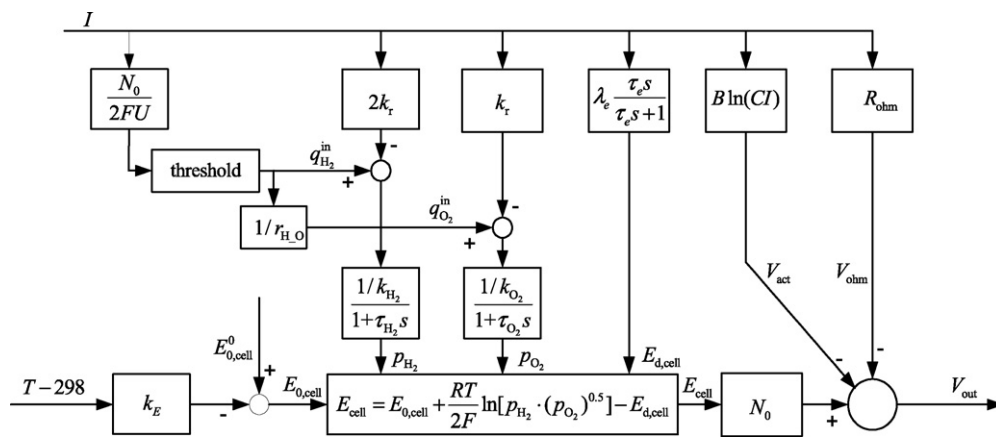


Fig. 3. PEMFC model.

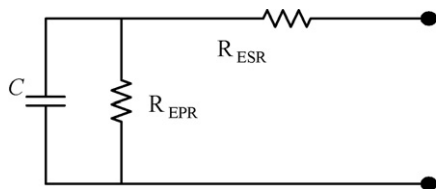


Fig. 4. Equivalent circuit model of the ultra-capacitor.

The real UC bank can be modeled by using multiple UC cells in parallel and series. The total resistance and capacitance of the UC bank are given by [9]:

$$R_{UCbank} = n_1 \frac{R_{ESR}}{n_2}, C_{UCbank} = n_2 \frac{C}{n_1} \quad (12)$$

4. Wavelet-transform-based power management strategy

There have been a variety of strategies capable of managing the power among different power sources. Fuzzy logic is well known to enhance conventional system design with engineering expertise, and the use of fuzzy logic can help to circumvent the requirement for rigorous mathematical modeling. Fuzzy logic supervisory control applied in multiple power sources of a HEV can avoid the low efficiency operation region of every power source and achieve high efficiency without degrading the mechanism performance. Ref. [6] proposed a power management strategy based on the fuzzy logic supervisory system for a fuel cell/ultra-capacitor/battery combined electric vehicle, whose objectives are to improve the performance of individual power sources and to ensure high power quality desirable for a good performance for electrical loads. Another power management strategy, adaptive control method, was presented in [7] for hybrid FC/battery power sources. In this adaptive control system, the hybrid power sources are optimized so that the fuel cell provides the energy required by the load, while the battery satisfies the peak power demands of the load. The output current of the fuel cell is adjusted according to the charge level of the battery. By this means, the fuel cell can achieve high efficiency, and the battery will not run down to depletion.

The power management strategies mentioned above have been proven effective in dealing with system efficiency. However, they fail to address the lifetime of the fuel cell stack and battery due to the dramatically negative impact of the frequent and rapid load demand variations in real world drive cycles. The lifetime of the fuel cell is a critical factor for HEV economy. So the questions of how

to avoid the rapid-variation and large-differential power demand for the fuel cell and how to appropriately distribute the power demands to power sources according to their natural characteristics arise. The wavelet transform (WT) can provide a potential solution. The WT decomposes an original signal into components at different positions and scales. It can be applied to extract signal information in both time and frequency domains. Wavelets with the property of localization are suitable for the analysis of non-stationary and transient signals [11–14]. Therefore WT can be employed as a very effective tool for the decomposition and detection of the transient features in 1-D seismic data, and similar data such as the power demand of the vehicle in this study. We extract the power transients from the total power demand and deliver them to the UC since the charging/discharging time of the UC can vary from several milliseconds to minutes. This measure protects the FC from the membrane damage resulting from the quick power demand variations. On the other hand, the battery absorbs the negative part of the rest power demand and shares the positive part with the FC. The FC does not have to provide the high peak power occasionally demanded by the load. As a result of using this WT-based power management strategy, the high efficiency of the FC can be achieved and the lifetime of the FC can be extended.

4.1. Algorithm analysis

The parameters used for WT-based algorithm analysis in this section are as follows: **G**, decomposition transfer function matrix; **H**, reconstruction transfer function matrix; K_ψ , constant determined by ψ ; t , time; u , position factor; W , wavelet coefficients; x , original signal; λ , scale factor; ψ , mother function.

The Morlet–Grossmann definition of continuous wavelet transform (CWT) for a 1-D signal $x(t)$ is described as

$$W(\lambda, u) = \int_R x(t) \frac{1}{\sqrt{\lambda}} \psi \left(\frac{t-u}{\lambda} \right) dt, \quad \lambda > 0, \quad u \in R \quad (13)$$

where λ is the scale parameter and u is the position factor. $\psi(t)$ is a mother function in both time domain and frequency domain called the mother wavelet. This mother wavelet is for the purpose of providing a source function to generate the daughter wavelets which are simply the translated and scaled versions of the mother wavelet. The inverse continuous wavelet transform can be exploited to recover the original signal $x(t)$,

$$x(t) = \frac{1}{K_\psi} \int_{R^+} \int_R W(\lambda, u) \frac{1}{\sqrt{\lambda}} \psi \left(\frac{t-u}{\lambda} \right) \frac{d\lambda du}{\lambda^2} \quad (14)$$

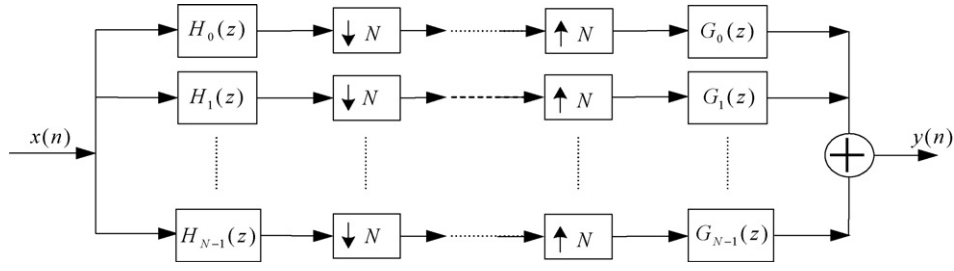


Fig. 5. Structure of Haar-wavelet-based N -channel filter bank.

As the most popular mother wavelet, the Haar wavelet has the shortest filter length in the time domain compared to other wavelets. Also, the Haar wavelet is the simplest possible wavelet with a nice feature that the WT is equal to its inverse [13]. With these features, the Haar wavelet makes the decomposition calculation much simpler than other wavelets do for realization of the wavelet-transform strategy in a realistic system. This can simplify the program composition and further improve the code execution efficiency. Meanwhile, the function of extracting transients can still be implemented well without degradation. Consequently the Haar WT is used in this paper for load profile decomposition to obtain the transients that are assigned for the ultra-capacitor. The Haar wavelet is expressed as

$$\psi(t) = \begin{cases} 1, & t \in \left[0, \frac{1}{2}\right) \\ -1, & t \in \left[\frac{1}{2}, 1\right) \\ 0, & \text{otherwise.} \end{cases} \quad (15)$$

Unlike CWT, the discrete wavelet transform (DWT) is used to decompose a discretized signal into different resolution levels. The DWT and its inverse are given by the following two equations respectively.

$$W(\lambda, u) = \int_{\mathbb{R}} x(t) \frac{1}{\sqrt{\lambda}} \psi\left(\frac{t-u}{\lambda}\right) dt \quad \lambda = 2^j, \quad u = k2^j, \quad j, k \in \mathbb{Z} \quad (16)$$

$$x(t) = \sum_{j \in \mathbb{Z}} \sum_{k \in \mathbb{Z}} W(j, k) \psi_{j,k}(t) \quad (17)$$

As shown in Fig. 5, by using the Haar-wavelet-based N -channel filter bank [14], the original signal $x(t)$ can be decomposed by a low-pass filter $H_0(z)$ and high-pass filters $H_k(z)$, $k = 1, 2, \dots, N-1$, into a reference signal and other detailed signals respectively. The reconstruction filters $G_k(z)$, $k = 0, 1, \dots, N-1$ are placed for signal reconstruction.

The decomposition transfer function matrix is expressed as

$$\mathbf{H} = \begin{bmatrix} H_1(z) \\ H_2(z) \\ \vdots \\ H_{N-1}(z) \\ H_0(z) \end{bmatrix} = \frac{1}{N} \begin{bmatrix} 1 & -1 & 0 & \dots & 0 & 0 \\ 0 & 1 & -1 & \dots & 0 & 0 \\ \vdots & \vdots & \vdots & \dots & \vdots & \vdots \\ 0 & 0 & 0 & \dots & 1 & -1 \\ 1 & 1 & 1 & \dots & 1 & 1 \end{bmatrix} \begin{bmatrix} 1 \\ z^{-1} \\ \vdots \\ z^{-N+2} \\ z^{-N+1} \end{bmatrix} \quad (18)$$

where z is the operator of the Z-transform.

The reconstruction filters are given by [14]

$$\mathbf{G} = \begin{bmatrix} G_1(z) \\ G_2(z) \\ \vdots \\ G_{N-1}(z) \\ G_0(z) \end{bmatrix} = \begin{bmatrix} N-1 & N-2 & \dots & 1 & 1 \\ -1 & N-2 & \dots & 1 & 1 \\ \vdots & \vdots & \dots & \vdots & \vdots \\ -1 & -1 & \dots & -N+2 & 1 \\ -1 & -2 & \dots & -N+1 & 1 \end{bmatrix}^T \begin{bmatrix} z^{-N+1} \\ z^{-N+2} \\ \vdots \\ z^{-1} \\ 1 \end{bmatrix} \quad (19)$$

The number of wavelet decomposition levels has to be considered properly complying with calculation simplicity and frequency restrictions as well in a realistic system. This number is analyzed and eventually determined to be three. Detailed analysis can be found in Part C of this section. Consider $N=2$, then the decomposition and reconstruction filters become $[H_1(z), H_0(z)]^T$ and $[G_1(z), G_0(z)]^T$, respectively. The three-level Haar wavelet decomposition and reconstruction are used for input signal $x(t)$. As shown in Fig. 6, the down-sampling and up-sampling methods are employed in the decomposition and reconstruction processes respectively. The data size reduces by half in down-sampling operations while it doubles in up-sampling operations.

4.2. Power demand sharing structure

Advanced simulation tool is employed to help set up a power demand model of the proposed power management system in an

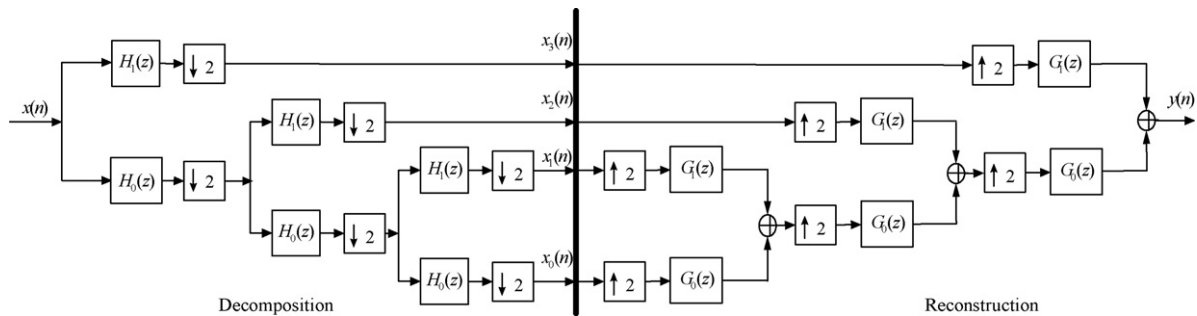


Fig. 6. Three-level Haar decomposition and reconstruction diagram.

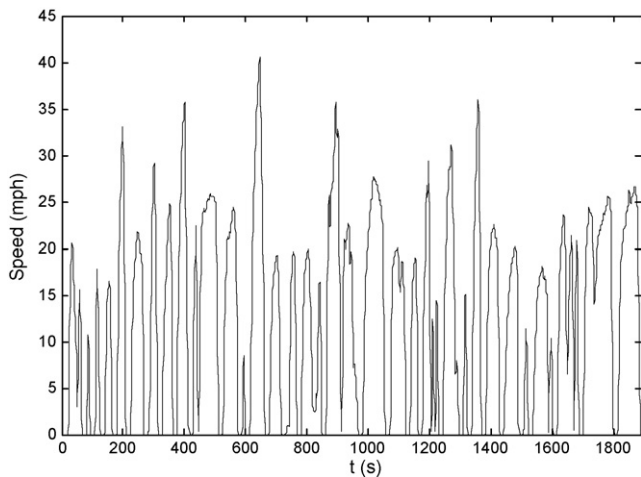


Fig. 7. Speed curve of OCC.

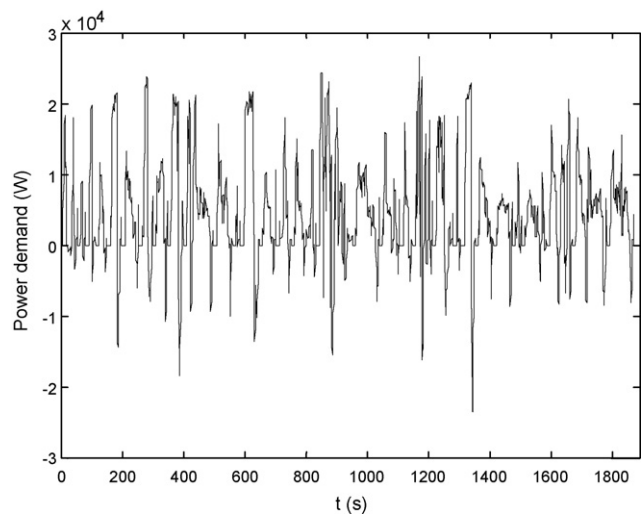


Fig. 8. Load profile of OCC.

HEV. The Orange County Cycle is chosen as a desired cycle for modeling. The speed curve during the OCC is drawn in Fig. 7. The power demand of the OCC driving cycle is shown in Fig. 8. For the convenience of design, the load profile is considered as the power demand. It can be seen from Fig. 8 that the load profile consists of many transients derived from the speed variations. By using

the Haar-wavelet-transform-based scheme, this power demand is divided into three parts for power distribution, which can take advantage of the three sources (i.e. the FC, UC and battery). The WT can properly deal with the nonlinear and uncertain transients.

The principle depicted in Fig. 6 is considered as a basis for the power sharing strategy. $H_0(z)$ is a low-pass filter and $H_1(z)$ is a high-pass filter. The original signal $x(n)$ equals the predetermined power demand of the OCC. As shown in Fig. 6, after three-level low-pass processing, the smooth slow-variation signal $x_0(n)$ is obtained as the power demand for the FC and battery. Other transients ($x_1(n) + x_2(n) + x_3(n)$) are distributed to the UC as mentioned above. However, $x_0(n)$ contains a negative part, which the FC cannot accept. Thus, the battery absorbs the slow-variation power with the direction from the load to power sources. The battery also helps absorb a portion of the positive low-frequency components, while the FC deals with the significant portion. So the power sharing method is expressed as below:

$$P_{FC}^* = \begin{cases} 0.6x_0(n) & \text{if } x_0(n) > 0 \\ 0 & \text{otherwise} \end{cases} \quad (20)$$

$$P_{\text{Battery}}^* = \begin{cases} 0.4x_0(n) & \text{if } x_0(n) > 0 \\ x_0(n) & \text{otherwise} \end{cases} \quad (21)$$

$$P_{UC}^* = x_1(n) + x_2(n) + x_3(n) \quad (22)$$

Based on this sharing strategy, the power demands for the FC, battery and UC are obtained and shown in Fig. 9(a)–(c), respectively. It can be observed that the power demand curve for the FC has global low frequency using the Haar wavelet decomposition, while at some time instants, fast power demand for the FC still exists. However, the number of large and fast power variations reduces dramatically, and the required surge power for the FC also decreases largely because of the assistance of the battery (compare Fig. 9(a) with Fig. 8). Consequently, the FC connected to a power converter with appropriate capacity and fast response can handle this power demand. The lifetime of the FC is extended consequently, which is a major advantage for utilization of the Haar wavelet transform in HEV power management.

4.3. Data acquisition and control system

For the three-level wavelet transform (see Fig. 6), the power variation frequency of the FC and battery is only 1/8 of that of the UC, so only eight sampling power points need to be foreknown for every calculation in power demand decomposition. The power demand studied in this paper is already known due to the predefined drive cycle. By using the power prediction algorithm [25] considering the vehicle speed and motor operation period, we can easily implement

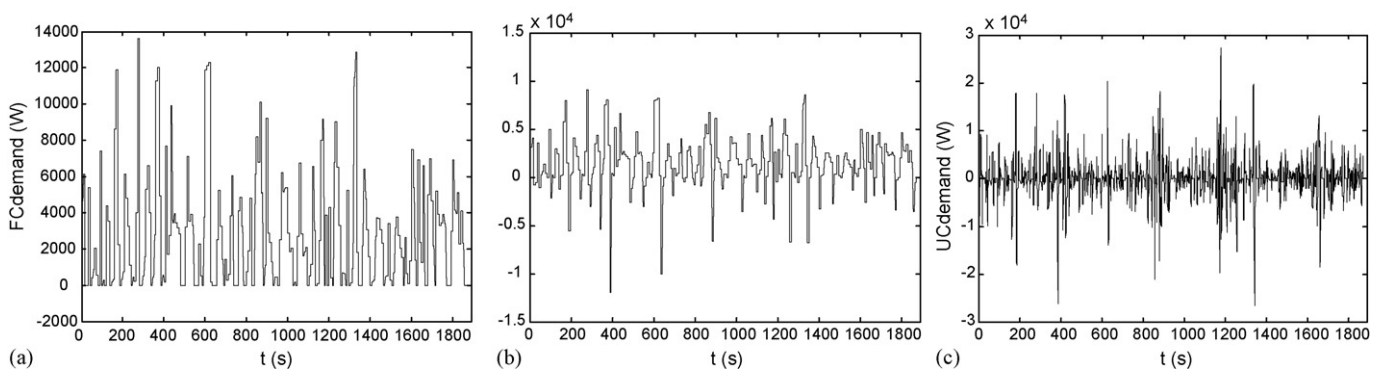


Fig. 9. Power components for the three power sources. (a) Power demand for FC. (b) Power demand for battery. (c) Power demand for UC.

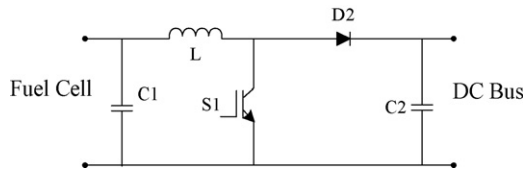


Fig. 10. Unidirectional DC/DC converter connected between FC and DC bus.

the real time power management for a running HEV. The calculation size is not large enough so that even a single-chip-machine can handle it.

As shown in Fig. 10, an isolated gate bipolar transistor (IGBT) S1 is employed in the topology of the unidirectional boost DC/DC converter for power tracking of the FC as mentioned in Section 2. The power from the fuel cell to the DC bus can be determined by inputting proper PWM drive signals to S1. By adding IGBT S2 and diode D1, the unidirectional DC/DC converter changes to a bi-directional converter, as shown in Fig. 11. For power tracking applications of the battery and UC as described in Section 2, the battery and UC are located on the V_{low} side, and the other side V_{high} is connected to the DC bus. So the voltage from the power sources is boosted on the DC bus with the aim of voltage regulation, the DC bus is placed on the V_{high} side and the load is linked to the V_{low} side. The DC load voltage is regulated to a constant approaching the power sources' voltage values.

The presence of DC/DC converters may increase the system cost and volume compared to the direct connected hybrid systems [26]. But by using DC/DC converters, the FC module size can be optimized. The FC is also protected from high-frequency and surge load power demand. Therefore the life expectancy can be extended. Meanwhile, the regenerated energy is properly restored due to the existence of UC and battery.

In this proposed power management system (see Fig. 1), the three power sources (i.e. FC, battery and UC) and corresponding power flow control are independent. The required power demand suitable for the characteristics of an individual power source can be met precisely. The specific control concepts are described below:

- The three-level Haar wavelet transform is utilized for decomposition of the HEV power demand.
- The PEMFC module deals with the majority of the positive portion of the low-frequency components of power demand derived from the wavelet decomposition. The power flow from the FC is determined by switch duty cycle of the unidirectional DC/DC converter. The duty cycle is obtained by the DAQ and control system.
- The battery satisfies the negative portion (during regeneration) and some of the positive portion of the low-frequency components of power demand derived from the wavelet decomposition. The battery not only absorbs the slow-variation power from the load but also helps the FC provide the required power to reduce the burden of the FC.
- All the high-frequency components of the power demand are met by the ultra-capacitor. The amount and direction of required

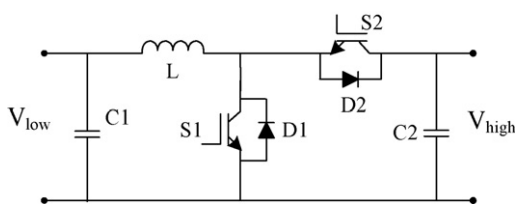


Fig. 11. Bi-directional DC/DC converter topology.

Table 1
PEMFC module parameters

FC stack temperature, T [K]	338
Number of FCs in series, N_0	353
Faraday's constant, F [C kmol ⁻¹]	96,484,600
Hydrogen time constant, τ_{H_2} [s]	3.37
Oxygen time constant, τ_{O_2} [s]	6.74
Hydrogen valve molar constant, k_{H_2} [kmol (atm s) ⁻¹]	4.22×10^{-5}
Oxygen valve molar constant, k_{O_2} [kmol (atm s) ⁻¹]	2.11×10^{-5}
Hydrogen–oxygen flow ratio, r_{H-O}	1.1679
Standard reference potential per cell, $E_{0,cell}^0$ [V]	0.6
Empirical constant in calculating open cell voltage, k_E [VK ⁻¹]	0.00085
Overall flow delay, τ_e [s];	80
Constant factor in calculating $E_{d,cell}$, λ_e [Ω]	0.00333
Gas constant, R [(mol K) ⁻¹]	8314.47
Constant to calculate the activation over voltage, B [A ⁻¹]	0.0478
Constant to calculate the activation over voltage, C [V]	0.0136
Utilization rate, U	0.85
Internal resistance, R_{ohm} [Ω]	0.004

fast-variation power is determined by properly controlling an individual switch existing in the bi-directional DC/DC converter. The switch status and switch duty cycle are outputs of the DAQ and control system.

- When the SOC of the battery drops to 0.5 because of over-discharging, switch S_{bat} in Fig. 1 turns on (i.e. connected to the upper diode attached to FC) until the battery voltage reaches the FC module terminal voltage. During this process, the battery is charged through the diode D_{bat} and switch S_{bat} . At this time switch S_{bat} is turned on and the battery is then charged from the FC module. When the SOC of the UC decreases to 0.25, switch S_{UC} in Fig. 1 turns on (i.e. connects to D_{UC}) until the UC voltage reaches the FC module terminal voltage. The UC is then charged from the FC module, thus avoiding the voltage collapse.
- If the SOC of the battery or UC increases to 0.95, the other two power sources (the UC and FC, or the battery and FC) are removed from the power train, and the battery or UC satisfies all the power demand as the only power source until its SOC drops to 0.85.
- The output current from the FC module is limited to its maximum value. Meanwhile, the battery and UC are initially charged to sufficient voltage, and the battery and UC are also charged from the load during the energy regeneration process. Thus, the SOC of the UC/battery will not decrease widely and the voltage difference between the FC and battery/UC will be within an acceptable range when the charging switch (S_{bat} or S_{UC}) turns on. These measures and conditions guarantee that the destructive surge current can be avoided.

5. Simulation results

5.1. Verification of power source models

The fuel cell parameters are derived from the data obtained of a fuel cell module [28]. According to the parameters shown in Table 1, the open cell voltage $E_{0,cell} = E_{0,cell}^0 - k_E(T - 298) \approx 0.6$ V. The no-load terminal voltage of the FC module is reconstructed to be 212 V, so the number of FCs in series is $N_0 = 353$. To completely satisfy the load demand shown in Fig. 8(a), two FC modules are connected in parallel. The rated output power per cell is 27.3 W. As a result, the rated power of the FC system is 19.3 kW. Consequently, the required power in Fig. 9(a) can be completely satisfied.

The lithium-ion battery parameters are shown in Table 2, which are based on experimental data from a 18650 lithium battery cell. The nominal voltage of this battery is 3.7 V. Accordingly the number of batteries in series is calculated to be 58 since the terminal voltage of the battery stack is 212 V in our design. To obtain the

Table 2
Lithium-ion battery parameters

Ambient temperature	23 °C
Parameters referring to the thermal model	$A = 4.3E-3 m^2$, $m = 41 g$, $c_p = 925 J kg^{-1} / K3 V^{\circ} C^{-1}$, $h_c = 10 W m^{-2} K^{-1}$
Parameters referring to the equivalent electrical circuit	$R_1 = 80 m\Omega$, $C = 4 F$, $R_2 = 40 m\Omega$, $v = 4.2 V$
Parameters for calculating the state of discharge	$\alpha_{\text{charg}} = 0.93$, $\alpha_{\text{discharg}} = 1.05$, $\beta = 1$
Potential correction	$\Delta E = 0 V$

Table 3
Ultra-capacitor parameters

Dimensions [mm]	164 × 62 × 62
Capacitance C [F]	2700
Equivalent series resistance R_{ESR} [Ω]	0.00085
Maximum float voltage [V]	2.3

sufficient current outputting ability, we place forty 18650 lithium battery cells in parallel. Additionally the nominal capacity of an 18650 lithium battery cell is 1.4 Ah, and the reference current for battery modeling is set to 1.4 A. So the nominal power of the battery stack is 12 kW. Meanwhile the maximum current of the US18650 battery can reach a few tens of amperes. Thus the maximum instantaneous power of the stack exceeds 100 kW. The analysis shows that this simulated battery stack can completely meet the requirements delineated in Fig. 9(b).

The ultra-capacitor specifications are given in Table 3. The maximum float voltage is 2.3 V. Therefore 105 UC cells are chosen so that the terminal voltage of the UC bank is equal to 212 V. The total UC internal resistance $R_{\text{UCbank}} = 0.00085 \times 105 = 0.0892 \Omega$ and the total capacitance $C_{\text{UCbank}} = 2700/105 = 25.71 F$. The rated current of the UC bank is 400 A. Therefore the maximum output power is larger than $400 \times 212 = 84.8 kW$. This can adequately satisfy the power demand depicted in Fig. 9(c).

The measured and simulated $V-I$ characteristics curves of the FC power module, the charging/discharging $V-t$ curves of the lithium-ion battery cell and the UC charge/discharge voltage curves are shown in Figs. 12–14, respectively. The observation that the simulation results are very close to the measurement data indicates that the power source simulation models are valid and accurate.

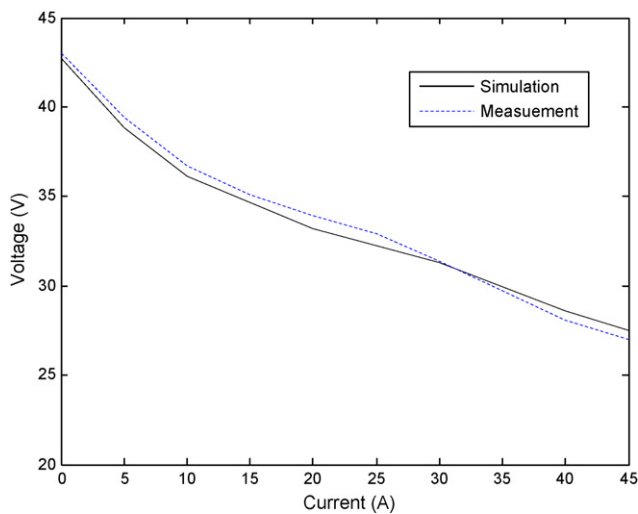


Fig. 12. Comparison of the simulated and measured $V-I$ characteristics curves of the FC power module.

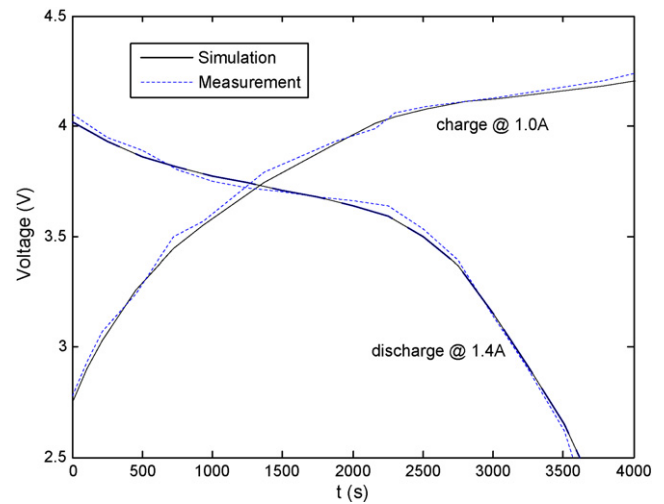


Fig. 13. Comparison of simulated and measured discharging/charging voltage variations of a lithium-ion battery.

5.2. Validation of power sharing algorithm

Figs. 15–18 show the voltage variations of the FC system, battery stack, UC and DC load side. Due to the required power, the voltages of the three power sources change accordingly. The battery shows good voltage stabilization performance in the whole drive cycle except a few moments. The increase in assigned power decreases the FC terminal voltage. The UC terminal voltage increases from 197 to 215 V as a whole because of regenerative energy. The DC voltage on the load side remains at 200 V with the help of the bi-directional DC/DC converter for voltage regulation.

The power tracking performance of the three power sources (i.e. the FC, battery and UC) is shown in Figs. 19–21. By comparing these power tracking curves to the required power curves shown in Fig. 9, it is found that the power demands are adequately satisfied. The power variations are within the maximum limitations of the power sources as mentioned above. According to Fig. 21, the UC absorbs the entire 110 kJ energy for a small-scale voltage increase, which conforms to Eq. (11). The SOC of the UC during such a drive cycle is within the desired range (<0.95), so no extra action is needed. However, if the SOC of the UC increases to 0.95, the other two power

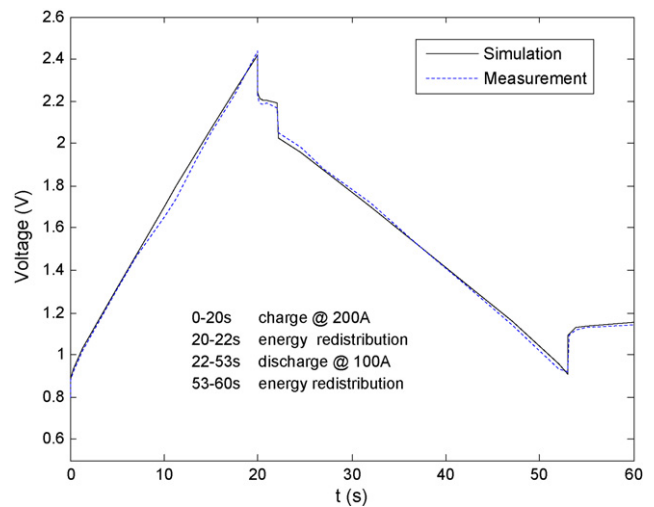


Fig. 14. Comparison of simulated and measured UC voltage during a period including charging and discharging.

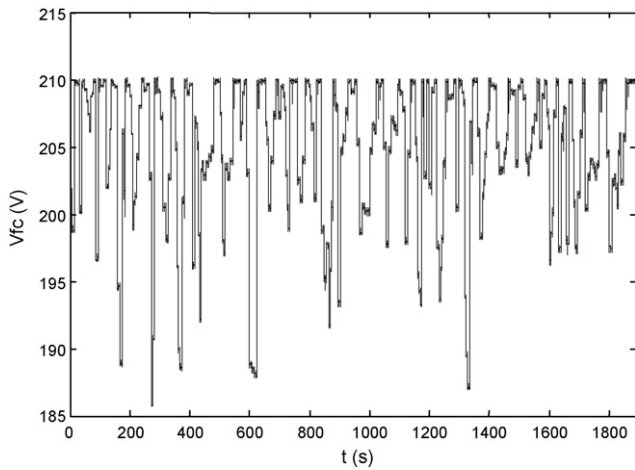


Fig. 15. FC terminal voltage.

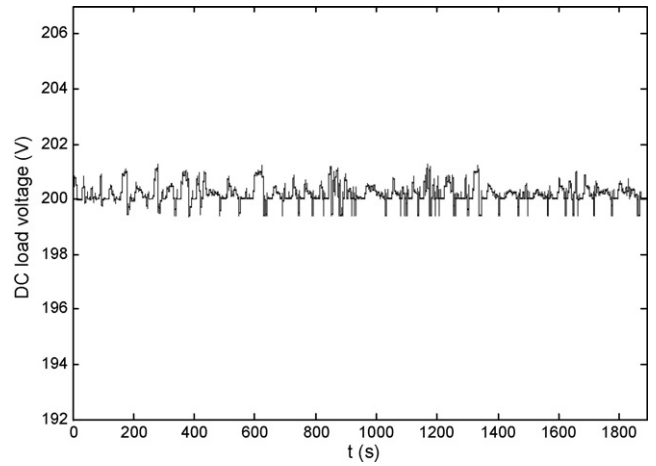


Fig. 18. Regulated DC load voltage.

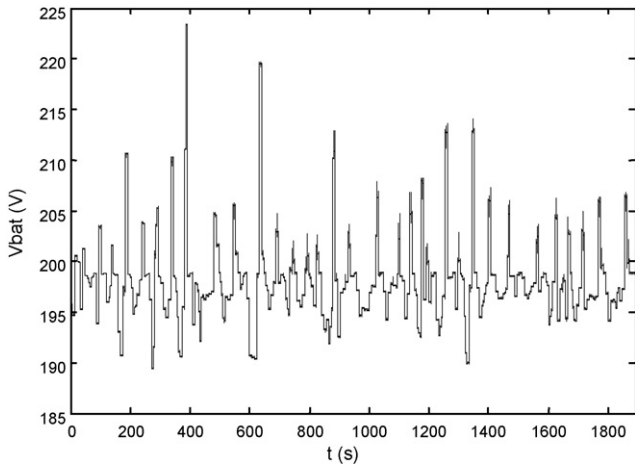


Fig. 16. Battery terminal voltage.

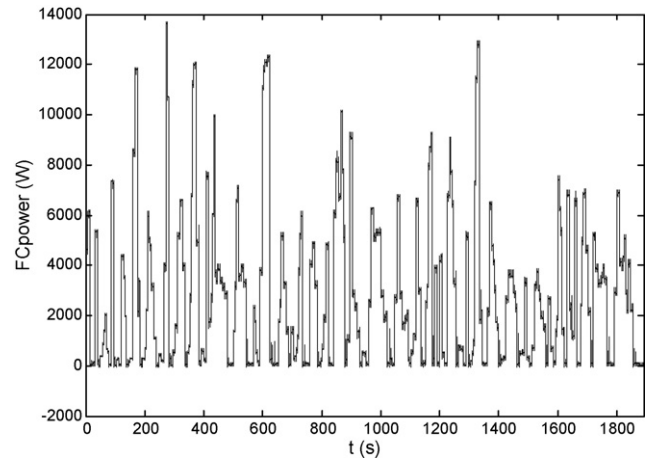


Fig. 19. FC output power.

sources (the battery and FC) will be removed in connection from the power train until the SOC of the UC drops to 0.85. The fact that the DC output power trajectory matches the load profile as shown in Fig. 8 proves the validity and correctness of the proposed power-sharing algorithm as evidenced in Fig. 22.

6. Experimental results

A scaled-down experimental setup was developed in the laboratory to validate the proposed algorithm. The power sources consist of a 1.2 kW fuel cell module (the rated operating voltage is 26 V),

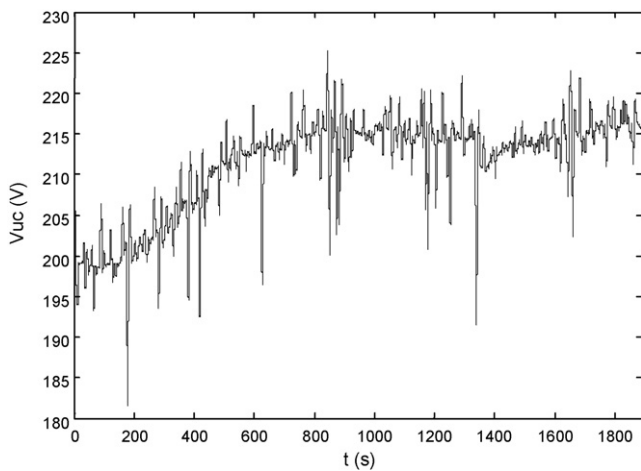


Fig. 17. UC terminal voltage.

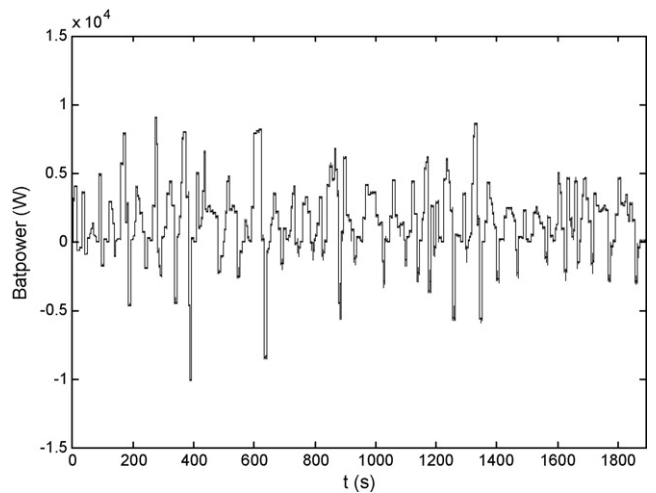


Fig. 20. Charging and discharging power of battery.

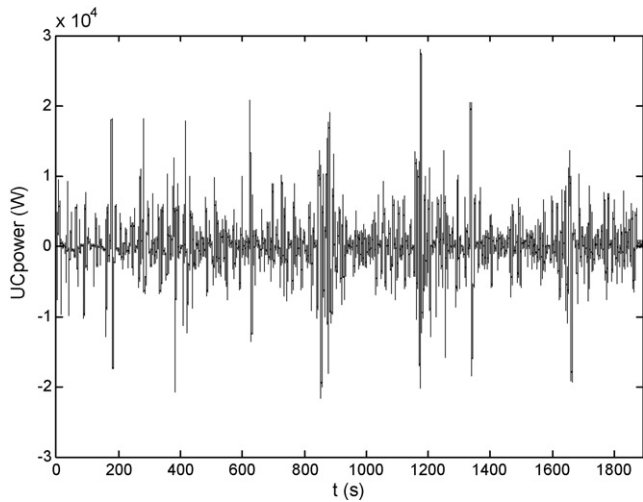


Fig. 21. Charging and discharging power of ultra-capacitor.

a lithium-ion battery pack ($V_{\text{nominal}} = 25.2 \text{ V}$, $C = 32.4 \text{ Ah}$) and an ultra-capacitor (the capacitance is 95 F). For the sake of simplicity of experimental verification, a certain time interval (971st–1000th second) is extracted from the OCC drive cycle to be analyzed. Meanwhile the power demand is scaled down because the power source voltage is low and the current cannot exceed some value due to the device limitation. The power demand in the experiment is 1/20 of that in the real OCC drive cycle, which is implemented by an electronic load ($P_{\text{max}} = 2.6 \text{ kW}$) operating as a load emulator. Three DC/DC converters controlled by a real time controller board are connected to three power sources respectively, switching at 10 kHz. The control program is compiled and downloaded to the real time controller board for sending and receiving signals. Currents and voltages are monitored and fed back into the controller board where the power is calculated as a product of the current and voltage. The real instantaneous power (in form of analog voltage) can be measured via DAC ports on the real time controller board.

The ideal power demand and the real power consumed by the electronic load are shown and compared in Fig. 23. The electronic load shows good power tracking precision to guarantee persuasion of experiments. The designed 1 kW hardware prototype is capable of meeting the requirement since the maximum power demand is

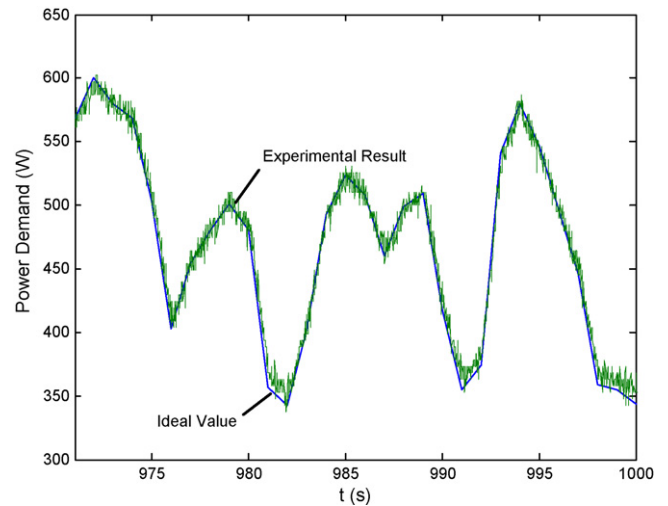


Fig. 23. Downscaled total power demand at a certain time interval of OCC.

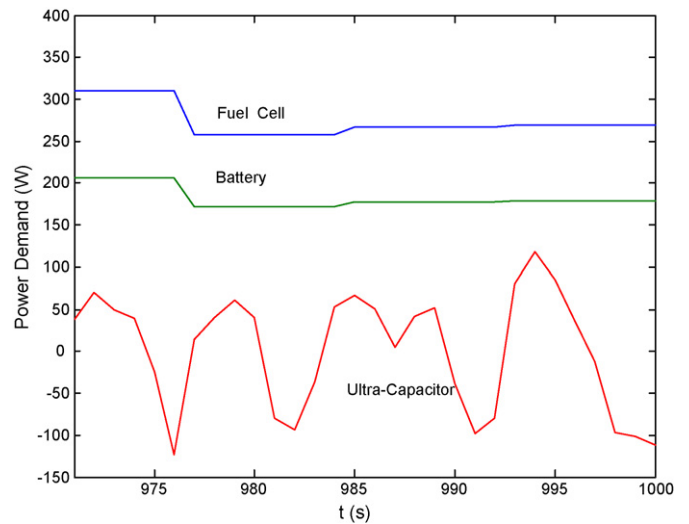


Fig. 24. Calculated power distribution for three power sources.

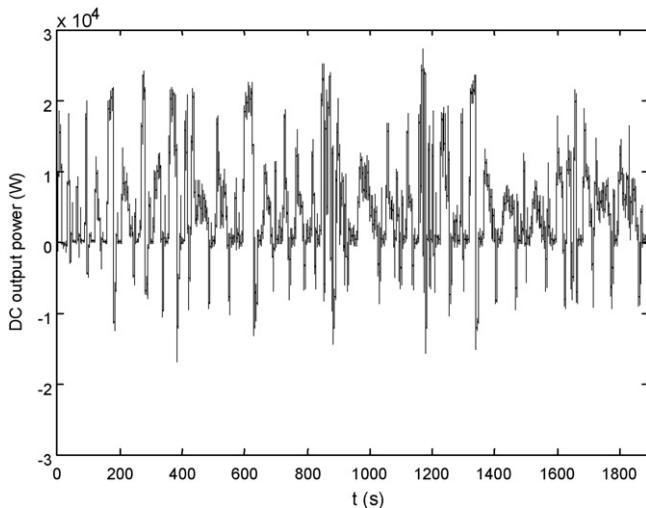


Fig. 22. Total output power for load demand.

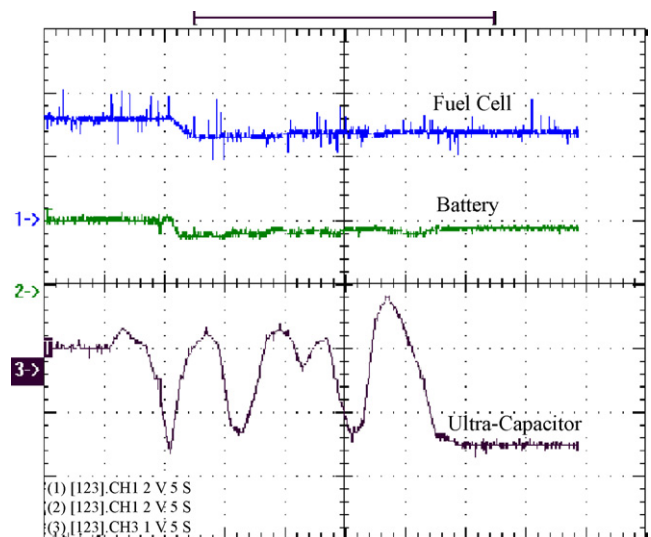


Fig. 25. Experimental results of power distribution.

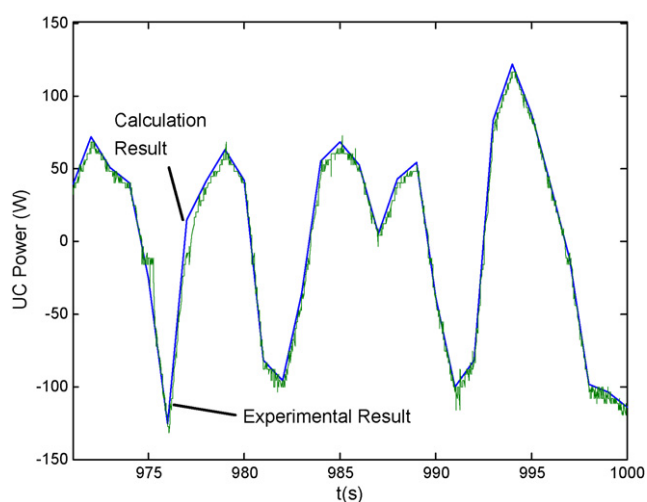


Fig. 26. Comparison of UC power between calculation and experimental results.

600 W. The power demands allocated to the fuel cell, battery and ultra-capacitor are calculated using the proposed wavelet transform and shown in Fig. 24. It can be seen that the high-frequency components are assigned for the UC, while the FC and battery cooperate with each other to share the low-frequency components obeying the aforementioned principle (see Eqs. (20) and (21)). Fig. 25 shows the measured waveforms of power possessed by the FC, battery and UC, respectively. To sufficiently prove validity of the experimental setup, the measured UC power is compared to the calculated UC power in Fig. 26 with the same scale. High similarity between the experimental result and the theoretical value exists not only during the positive power transferring process (outputting power) but also during the negative power transferring process (absorbing power). Consequently, the experimental results validate that the proposed wavelet-transform-based power sharing algorithm is applicable to the real hardware environment.

7. Conclusion

With the proposed wavelet-transform-based power management algorithm, the decomposed components of the load profile during a drive cycle can be distributed to the FC, battery and UC, compatible with their respective characteristics in order to obtain satisfactory performance. The lifetime of the FC module can be significantly increased and its cost can be dramatically reduced by using the architecture and algorithm proposed in the paper. This is because the UC deals with the fast-variation transient and peak power demand, while the battery helps the FC satisfy the low-frequency portion, with the latter absorbing the majority of the

power demand in the normal running process except acceleration or deceleration. The proposed power management system was implemented using a modeling and simulation software platform. Experimental data has been validated against the simulated data, thus verifying the accuracy of the power source models. The simulation results also verify the validity of the power-sharing algorithm. Real time controller based experiments demonstrate the applicability of the proposed strategy to the real system.

References

- [1] L.C. Iwan, R.F. Stengel, *IEEE Trans. Veh. Technol.* 50 (January (1)) (2001) 125–143.
- [2] S. Aso, M. Kizaki, Y. Nobobe, Development of Fuel Cell Hybrid Vehicles in TOYOTA, in PCC'07, Nagoya, April 2–5, 2007, paper 2007-37-3139.
- [3] T. Matsumoto, No. Watanabe, H. Sugiura, T. Ishikawa, SAE World Congress, Detroit, MI, March 4–7, 2002, paper 2002-01-0096.
- [4] Y. Wu, H. Gao, *IEEE Trans. Veh. Technol.* 55 (November (6)) (2006) 1748–1755.
- [5] T. Markel, M. Zolot, K.B. Wipke, A.A. Pesaran, Advanced Automotive Battery Conf., Nice, France, June 10–13, 2003.
- [6] A.A. Ferreira, J.A. Pomilio, G. Spiazzi, L.D.A. Silva, *IEEE Trans. Power Electron.* 23 (January (1)) (2008) 107–115.
- [7] Z. Jiang, L. Gao, R.A. Dougal, *IEEE Trans. Energy Conserv.* 22 (June (2)) (2007) 507–515.
- [8] A.C. Baisden, A. Emadi, *IEEE Trans. Veh. Technol.* 53 (January (1)) (2004) 199–206.
- [9] A. Kotsopoulos, J.L. Duarte, M.A. Hendrix, *IEEE International Symposium on Industrial Electronics*, vol. 2, 2004, pp. 4–7.
- [10] G. Wenzhong, *IEEE Trans. Veh. Technol.* 54 (3) (May 2005) 846–855.
- [11] G. Bachman, L. Narici, E. Beckenstein, *Fourier and Wavelet Analysis*, Springer, New York, 2000.
- [12] B.J. Falkowski, *Electron. Lett.* 34 (May (11)) (1998) 1084–1085.
- [13] T.Q. Nguyen, P.P. Vaidyanathan, *IEEE Trans. Acoust. Speech Signal Process.* 38 (March (3)) (1990) 433–446.
- [14] X. Wang, *IEEE Trans. Image Process.* 15 (September (9)) (2006) 2771–2779.
- [15] L.J. Gao, Z.H. Jiang, B.A. Dougal, *IEEE Trans. Aerosp. Electron. Syst.* 41 (January (1)) (2005) 348–355.
- [16] A. Davis, Z.M. Salameh, S.S. Eaves, *IEEE Trans. Energy Convers.* 14 (June (2)) (1999) 245–250.
- [17] C. Fellner, J. Newman, *J. Power Sources* 85 (February (2)) (2000) 229–236.
- [18] T. Horiba, K. Hironaka, T. Matsumura, T. Kai, M. Koseki, Y. Muranaka, *J. Power Sources* 97–98 (July) (2001) 719–721.
- [19] L. Gao, S. Liu, R.A. Dougal, *IEEE Trans. Comp. Packag. Technol.* 25 (September (3)) (2002) 495–505.
- [20] D. Bernardi, E. Pawlikowski, J. Newman, *J. Electrochem. Soc.* 132 (1) (1985) 5–12.
- [21] C.E. Chamberlin, *J. Electrochem. Soc.* 142 (August (8)) (1995) 2670–2674.
- [22] M.Y. El-Sharkh, A. Rahman, M.S. Alam, P.C. Byrne, A.A. Sakla, T. Thomas, *J. Power Sources* 138 (1/2) (2004) 199–204.
- [23] C. Wang, M.H. Nehrir, S.R. Shaw, *IEEE Trans. Energy Convers.* 20 (June (2)) (2005) 442–452.
- [24] G. Maggio, V. Recuperio, L. Pino, *J. Power Sources* 101 (October (2)) (2001) 275–286.
- [25] R. Beck, A. Bollig, D. Abel, *Oil Gas Sci. Technol.* 62 (July/August (4)) (2007) 635–643.
- [26] P. Bentley, D.A. Stone, N. Schofield, *J. Power Sources* 147 (September (1/2)) (2005) 288–294.
- [27] K.B. Wipke, M.R. Cuddy, S.D. Burch, *IEEE Trans. Veh. Technol.* 48 (November (6)) (1999) 1751–1761, Special Issues on Hybrid and Electric Vehicles.
- [28] Hal H Ottesen, Dynamic Performance of the Nexa Fuel Cell Power Module, <http://www.interstatetraveler.us/Reference-Bibliography/Dynamic%20Fuel%20Cell%20Performance%20Final%20Jan%202004%20U%20of%20M%20Rochester%20MN.pdf>, last visited by the author on June 20, 2008.